1   **Tunable drug release from nanofibers coated with blank**

2   **cellulose acetate layers fabricated using tri-axial electrospinning**

3   Yaoyao Yang [a,1], Wenbing Li[b,1], Deng-Guang Yu [a,*], Guanhua Wang [b], Gareth R.
4   Williams [c] and Zhu Zhang [d,*]

5   [a] School of Materials Science & Engineering, University of Shanghai for Science & Technology,
6   Shanghai 200093, China.
7   [b] School of Chemistry & Chemical Engineering, Wuhan University of Science & Technology,
8   Wuhan 430081, China
9   [c] UCL School of Pharmacy, University College London, 29-39 Brunswick Square, London WC1N
10   1AX, UK.
11   [d] Department of Internal Medicine, The Hospital of Wuhan University of Science & Technology,
12   Wuhan 430081, China

13
14   [1] These authors contributed equally to this work.
15

16

17

18

19   ***Corresponding authors:**
20   Prof. Deng-Guang Yu and Dr. Zhu Zhang
21
22   **Addresses**:
23   *DGY:*
24   School of Materials Science & Engineering,
25   University of Shanghai for Science and Technology,
26   516 Jungong Road, Yangpu District,
27   Shanghai 200093, P.R. China
28   **Tel./ Fax**: +86-21-55270632
29   **E-mail**: ydg017@usst.edu.cn
30
31   *ZZ:*
32   Department of Internal Medicine
33   The Hospital of Wuhan University of Science & Technology
34   Wuhan 430081, China
35   **E-mail**: zhangzhu75@wust.edu.cn
36
37

Abstract

In this study, novel core-shell nanostructures were fabricated through a modified triaxial electrospinning process. These comprised a drug-protein nanocomposite coated with a thin cellulose acetate (CA) shell. They were generated through the simultaneous treatment of an outer solvent, an unelectrospinnable middle fluid, and an electrospinnable core solution in triaxial electrospinning. SEM and TEM results revealed that the core-shell nanofibers had linear and cylindrical morphologies with a diameter from 0.66 to 0.87 μm, and distinct core-shell structures with a shell thickness from 1.8 to 11.6 nm. The presence of a CA coating eliminated the initial burst release of ibuprofen seen from a monolithic drug-protein composite, and allowed us to precisely manipulate the drug release (for a 90% percentage) over a time period from 23.5 to 43.9 h in a tunable manner. Mathematical relationships between the processing conditions, the nanostructures produced, and their functional performance were elucidated.

Chemical compounds studied in this article

Ibuprofen (PubChem CID: 3672); Gliadin (PubChem CID: 17787981); Cellulose acetate (PubChem CID: 3084039); Methylene blue (PubChem CID: 6099); Basic fuchsin (PubChem CID: 12447); 1,1,1,3,3,3-hexafluoro-2-propanol (PubChem CID:13529); Trifluoroacetic acid (PubChem CID: 6422); Acetone (PubChem CID: 180); Acetic acid (PubChem CID: 176).

1. Introduction

The ability to fabricate structures with controllable nanoscale architectures has enabled the development of much new science and technology (Isaacoff & Brown, 2017), and is of vital importance in the development of new kinds of functional nanomaterials, particularly for biomedical fields (Hubbell & Chikoti, 2012; Mehta, et al., 2017; Haider, et al., 2018; Mitragotri, Burke, & Langer, 2014; Khoshnevisan, et al., 2018; Wen, et al., 2017). Beyond simple monolithic structures, where the composition is the same throughout, a range of more complicated nanostructures can be envisaged. Of these, the most widely explored by far is the core-shell (or core-sheath) structure, which contains separate and different core and shell compartments (Li, et al., 2018; Lu, et al., 2018). These can either both be solid-state phases (i.e., two different solids, one nested inside another), or the core could be a liquid or even a gas (giving a hollow material) (Chang, et al., 2017; Wang, et al., 2018; Mao, et al., 2018; Masoumifard, Guillet-Nicolas, & Kleitz, 2018; Nie, Fu, & Wang, 2010; He, et al., 2017; Eltayeb, Stride, & Edirisinghe, 2013; Lauhon, Gudiksen, Wang, & Lieber, 2002). A simple search in Web of Science using "core shell" as the topic reveals that 32,988 such studies (April 29, 2018) have been published within the last 5 years, equating to 18 publications on the topic per day. There are numerous methods which can be used to generate this simple structure, and some excellent reviews have focused on the preparation and application of core-shell materials (Chaudhuri & Paria, 2012; Qu, Wei, & Guo, 2013).

Electrospinning is a simple and straightforward process which can be used to

89 create nanofibers from polymer solutions or melts. It has attracted much attention in

90 the research literature because the resultant nanofibers have many advantageous

91 properties, such as large surface areas, high porosity, and a continuous 3-D web

92 structure (Jiang, Uch, Agarwal, & Greiner, 2017; You, et al., 2018; Wang, et al., 2017;

93 Habiba, et al., 2018; Szabó, et al., 2018; Wali, et al., 2018). The process involves the

94 ejection of a polymer solution through a needle, termed the spinneret, towards a

95 collector plate. A high potential difference is applied between the two, resulting in the

96 conversion of the initial solution into 1-D nanofibers. The macrostructure of the

97 spinneret is mirrored in the products of electrospinning, allowing the generation of

98 complex nanostructures if the process is fully optimized. Such structures include

99 core/shell and Janus (side-by-side) architectures, as well as combinations of the two.

100 Electrospun materials are produced in a single step, and thus intricate nanoscale

101 architectures can be fabricated in a straightforward manner through the simultaneous

102 treatment of multiple working fluids in a direct and top-down manner (Zhao, Cao, &

103 Jiang, 2007; Starr, Budi, & Andrew, 2015; Han & Steckl, 2013; Jiang, et al., 2014;

104 Labbaf, Ghanbar, Stride, & Edirisinghe, 2014; Liu, Ni, Chase, & Rabolt, 2013; Yu, Li,

105 Williams, & Zhao, 2018; Lallave, et al., 2007; Jiang, et al., 2018).

106   The traditional single-fluid blending electrospinning process uses a single

107 solution to generate monolithic fibers, and accounts for over 95% of the publications

108 concerning electrospinning. However, although it is more complex to implement

109 experimentally, the simultaneous treatment of multiple fluids greatly increases the

110 capability of electrospinning to develop new functional nanomaterials. In a

111 single-fluid electrospinning process, the working fluid must be electrospinnable,

112 which limits the range of systems which can be worked with. It is estimated that only

113 around 100 different polymers can be electrospun into nanofibers, and even then they

114 can only be processed within a narrow window of conditions (solvent, concentration,

115 molecular weight, etc) (Agarwal, Greiner, & Wendorff, 2013). In multiple-fluid

116 electrospinning processes, only one of the working fluids needs to be electrospinnable.

117 Hence, a very wide variety of unspinnable fluids, such as dilute solutions, solvents,

118 suspensions, and emulsions, can be processed into fibers with the aid of a spinnable

119 fluid companion.

120   Coaxial electrospinning, involving two liquids, one of which is nested inside

121 another, is by far the most widely explored multi-fluid electrospinning process. It can

122 be implemented with both solutions being spinnable, with a spinnable shell and

123 unspinnable core, or with a spinnable core and unspinnable shell (the latter process is

124 often termed "modified coaxial electrospinning"). The more complex triaxial process

125 (using three concentrically nested needles), while less studied, has also been

126 demonstrated to be useful in creating nanofibers with three-layer structures and

127 improved functional performance (Liao, et al., 2018; Zanjani, et al., 2017; Han,

128 Sherman, Filocamo, & Steckl, 2017; Liu, Ni, Chase, & Rabolt, 2013). Modified

129 triaxial electrospinning processes, where one of more of the fluids being processed is

130 not electrospinnable alone, have additionally been investigated (Yang, et al., 2016). A

131 series of situations can be envisaged depending on the electrospinnability of the outer,

132 middle, and inner working fluids. These processes proceed easily when two of the

133   three working fluids are electrospinnable and compatible with each other, but become

134   challenging when only one of the fluids is electrospinnable. The production of fibers

135   using a spinnable middle fluid combined with unspinnable outer and inner working

136   fluids has been successfully implemented (Yang, et al., 2017), but Yang et al.

137   previously hypothesized that using an electrospinnable core solution to support

138   unspinnable outer and middle working fluids is not possible (Yang, et al., 2016).

139   In this paper, we developed a modified triaxial electrospinning process involving

140   an electrospinnable core solution, and were able to successfully use this to support

141   both an unspinnable middle polymer solution and an unspinnable outer fluid

142   (comprising a pure solvent). As a result, we could fabricate high-quality core/shell

143   fibers using this process. The concentration of the middle-layer polymer solution was

144   varied to adjust the thickness of the sheath compartments in the fiber products,

145   allowing the drug release profile to be tuned.

146   **2. Materials and methods**

147   **2.1. Materials**

148   Ibuprofen (IBU; 2-(4-isobutylphenyl)propanoic acid), was used as a model poorly

149   water-soluble drug, and was procured from the Zheng-Zhou Chuang-Mei

150   Biotechnology Co., Ltd. (Zhengzhou, China). Gliadin (extracted from wheat) was

151   obtained from the Miao-Sheng Biotechnology Co., Ltd. (Shanghai, China). Cellulose

152   acetate (CA, M_w = 100,000 Da, the degree of substitution was 2.5) was sourced from

153   Acros (NJ, USA). Colorants (methylene blue and basic fuchsin) and organic solvents

154   (including 1,1,1,3,3,3-hexafluoro-2-propanol [HFIP], trifluoroacetic acid [TFA],

155 acetone and acetic acid) were of analytical grade and purchased from the Shanghai

156 Zi-Yi Chem. Co., Ltd. (Shanghai, China). Water was doubly distilled before use.

157 **2.2. Electrospinning equipment and working fluids**

158 The electrospinning apparatus was self-built, and a detachable trilayer concentric

159 spinneret was designed and manufactured in-house. Other components of the

160 equipment included three syringe pumps (two KDS100 and one KDS200,

161 Cole-Parmer, IL, USA), a high-voltage power supply (ZGF60kV/2mA, Wuhan

162 Hua-Tian Co., Ltd., Wuhan, China), and a flat piece of cardboard wrapped with

163 aluminum foil (employed as a collector). The electrospinning processes were

164 observed using a Canon camera (PowerShot SX50HS, Tokyo, Japan).

165 To prepare the inner working fluid, 4.0 grams of IBU were firstly placed into 100

166 mL solvent mixture of HFIP and TFA (8:2 v/v). Later, 16 grams of gliadin powders

167 were put into the drug solution, which was stirred using a magnetic stirrer for several

168 hours. The middle fluid was prepared by dissolving a certain amount of CA powders

169 into the mixture of acetone and acetic acid (2:1 v/v). The outer fluid was a plain

170 solvent of acetone and acetic acid (2:1 v/v).

171 **2.3. Morphology**

172 The morphological characteristics of the electrospun nanofibers were assessed with

173 the aid of a Quanta FEG450 scanning electron microscope (SEM; FEI Corporation,

174 Hillsboro, OR, USA). Prior to SEM observation, samples were sputter coated with

175 platinum under a nitrogen atmosphere to render them electrically conductive. Images

176 were recorded at an excitation voltage of 20 kV. The diameter distributions of the

177 fiber formulations were analyzed using the ImageJ software (National Institutes of

178 Health, Bethesda, MD, USA) to measure diameters at 100 different points in the SEM

179 images.

2.4. Internal structure

181 The internal structures of the electrospun nanofibers were studied using a

182 transmission electron microscope (TEM; JEM 2100F, JEOL, Tokyo, Japan) under an

183 excitation voltage of 300 kV. The samples were prepared by fixing a lacey

184 carbon-coated copper grid on the collector and spinning directly onto it for a few

185 seconds.

2.5. X-ray diffraction

187 The physical form of the raw materials (IBU, CA, and gliadin) and the nanofibers

188 were assessed with an X-ray diffractometer (XRD; D/Max-BR, RigaKu, Tokyo, Japan)

189 supplied with Cu Kα radiation at 40 mV and 30 mA. Patterns were collected over the

190 2θ range $5 - 60°$.

2.6. Infrared spectrometry

192 An attenuated total reflectance–Fourier transform infrared (IR) spectrometer

193 (Nicolet-Nexus 670, Nicolet Instrument Corporation, Madison, USA) was employed

194 to study the raw materials and electrospun formulations. Spectra were obtained over

195 the wavenumber range $500 - 4000$ cm^{-1} at a resolution of 2 cm^{-1}.

2.7. In vitro dissolution tests

197 Following the Chinese Pharmacopoeia (Method II), an RCZ-8A paddle instrument

198 (Tianjin University Radio Factory, Tianjin, China) was used for in vitro dissolution

199 tests (National Pharmacopoeia Committee, 2015). Before the tests were performed,

200 the apparatus was set to 50 rpm and 37 °C. One hundred milligrams of the medicated

201 nanofiber sample was placed into 600 mL of phosphate buffered saline (PBS, pH =

202 7.0, 0.1 mol/L). At predetermined time points, 5 mL aliquots were withdrawn from

203 the release medium, and 5 mL of fresh pre-headed PBS added to the dissolution

204 vessels to maintain a constant volume. The absorption of each sample was determined

205 at λ_{max} = 264 nm, with a Lambda 750S UV-vis spectrophotometer (Perkin Elmer,

206 Waltham, MA, USA). The cumulative amount of IBU released was back-calculated

207 on the basis of a predetermined calibration curve. The dissolution tests of each sample

208 were repeated six times, and results are reported as mean ± S.D.

209 **2.8. Statistical analysis**

210 The experimental data are presented as mean ± SD. The results from the *in vitro*

211 dissolution tests were analyzed using one-way ANOVA. The threshold significance

212 level was set at 0.05. Thus, *p* (probability) values lower than 0.05 were considered to

213 be statistically significant.

214
215 ### 3. Results and discussion

216 #### 3.1. Modified triaxial electrospinning

217 A schematic of the modified triaxial electrospinning equipment is shown in Fig. 1.

218 Similar to a traditional single-fluid electrospinning experiment, the system consisted

219 of four parts: the power supply, spinneret, collector, and fluid-driving pumps.

220 Traditional triaxial electrospinning (with all of the working fluids being

221 electrospinnable) treats three fluids simultaneously, and as a result can create

222 three-layer nanofibers (Han, Sherman, Filocamo, & Steckl, 2017; Liu, Ni, Chase, &

223 Rabolt, 2013). The modified tri-axial electrospinning approach explored in this work

224 greatly enhances the possibilities of generating novel materials, because there are only

225 a limited number of electrospinnable solutions but a virtually infinite range of

226 unspinnable liquids (Yang, et al., 2016; Yang, et al., 2017).
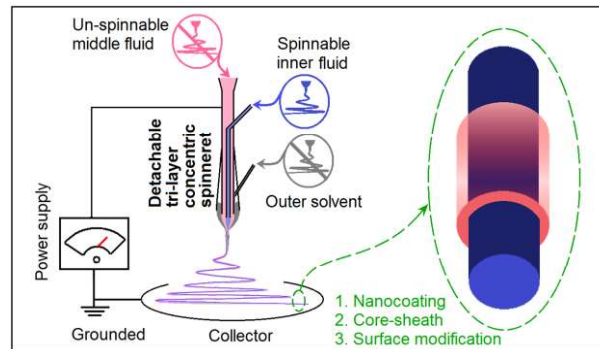
227

228 **Fig. 1** A schematic of the modified triaxial electrospinning process, and its potential

229 applications.

230 Here, two unspinnable liquids were implemented as the outer and middle

231 working fluids, with only the core solution being electrospinnable. The core

232 comprises a mixture of IBU and gliadin, while the middle fluid is a dilute CA solution,

233 and the outer liquid consists of acetone and acetic acid (2:1 v/v). The core solution is

234 spinnable and forms the fiber filaments, while the CA middle fluid is deposited on

235 this in the form of a thin "nanocoating". The outer solvent helps to ensure a stable and

236 continuous preparation process.

237 **The detachable triaxial spinneret.** A detachable triaxial spinneret was

238 developed to guide the three working fluids (Fig. 1 and Fig. 2). The assembly of the

239 detachable spinneret is exhibited in Fig. 2a. A traditional two-layer concentric metal

240 spinneret was inserted in a 2.4 cm length of tapering polypropylene (PP) tubing

241 (internal diameter and wall thickness: 1.84 - 2.5 mm and 0.3 mm, respectively), with

242 the wider end of the PP tube located at the spinneret exit (as illustrated in Fig. 2b).

243 The capillaries comprising the concentric metal spinneret had outer diameters and

244 wall thicknesses of 1.84/0.25 and 0.62/0.15 mm.
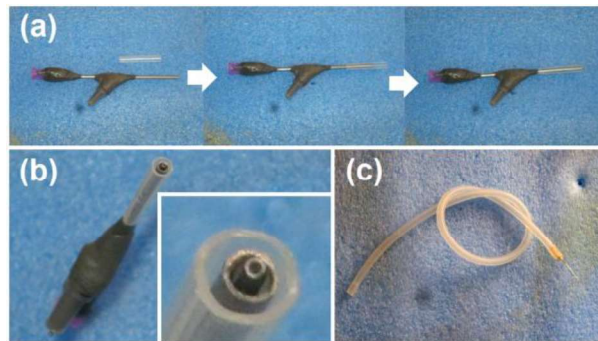
245

246 **Fig. 2** Photographs showing the homemade trilayer concentric spinneret: (a) a

247 traditional two-layer concentric metal spinneret was inserted in a tapering PP tube; (b)

248 the resulting trilayer concentric spinneret (inset: close-up of the exit nozzles); (c) the

249 silica tube and needle used for the transport of the outer working fluid.

250 A sharp needle (outer diameter / wall thickness: 0.3/0.05 mm) was connected to

251 a length of highly elastic silica tubing (Fig. 2c), which was then connected to the

252 syringe containing the outer working fluid. The outer layer working fluid was then

253 carried to the triaxial spinneret simply by inserting the metal needle through the PP

254 tube.

255 This set-up differs somewhat from more traditional triaxial spinnerets, which

256 usually consist of three concentrically nested metal capillaries. It offers three

257 advantages. First, the detachable spinneret can be easily prepared and washed after

258 use. This can be very challenging with one-piece metal spinnerets, especially when

259 the core needle is very narrow. Second, the PP tube at the exterior is likely to be more

260 efficient in utilizing the electrostatic energy provided by the high-voltage power

261 supply than an entirely metal spinneret, as has been demonstrated with Teflon-coated

262 concentric spinnerets in coaxial electrospinning (Wang, et al., 2018). Third, PP is an

263 excellent electrical insulator, and will have only minimal interactions with the

264 working fluids. In contrast, metal spinnerets are highly conductive, and there is the

265 potential for the liquids being expelled to interact with the spinneret to a certain extent,

266 rather than travelling directly to the collector and forming fibers. The PP surface thus

267 will have less negative effects on the exterior working fluid than a metal surface

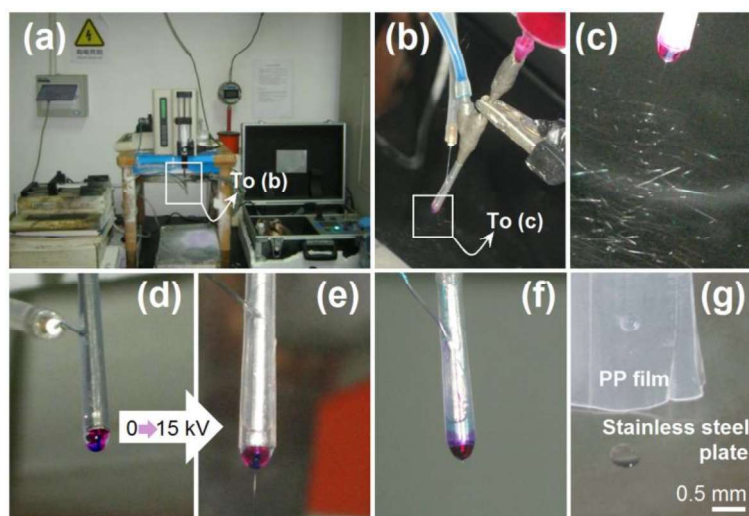268 would during the triaxial electrospinning process.

269 **3.2. Implementation of the modified triaxial electrospinning processes**

270 A photograph of the modified triaxial electrospinning system is illustrated in Fig. 3a.

271 The syringe containing the middle working fluid was directly connected to the

272 spinneret, while the inner fluid and the outer solvent were pumped to the spinneret

273 through the highly elastic silica gel tubes. Electrical energy was transferred to the

274 working fluids through an alligator clip fixed on the metal surface of the spinneret

275 (Fig. 3b).

276   Four different fiber formulations were prepared (Table 1). The first used a plain

277 solvent of acetone and acetic acid (2:1 v/v) for both the middle and outer fluids: hence,

278 although three fluids were being dispensed, two were the same, and the process

279 equated to modified coaxial electrospinning. As a result, the F1 fibers generated

280 comprise a monolithic composite with IBU dispersed throughout a gliadin matrix.

281   A typical modified triaxial electrospinning process (exhibiting a Taylor cone

282 followed by a straight fluid jet and then a whipping and bending region) is shown in

283 Fig. 3c for the preparation of the F3 formulation. In the absence of electrical charge,

284 the three working fluids formed a compound droplet (Fig. 3d), with the three layers

285 clearly visible because of the inclusion of methylene blue in the inner fluid (5×10^{-6}

286   g/mL) and basic fuchsin in the middle solution. When a voltage of 15 kV was applied,

287   a compound Taylor cone was formed (Fig. 3e). During the electrospinning processes,

288   a stable concave surface of the outer solvent within the PP tube can be observed. This

289   is more obviously when 5×10^{-7} g/mL methylene blue was added into the outer

290   solvent mixture (Fig. 3f). When a droplet of the outer solvent mixture (*ca.* 0.007 mg)

291   was added on a PP film and a stainless steel plate (consisting of 1Cr18Ni9, the same

292   as the metal capillaries), the droplet on the metal plate spread out more open than on

293   the PP film (Fig. 3g). This give a hint that the PP surface exerted smaller drawing

294   force on the working fluids than the stainless steel surface, favorable for the stable

295   and robust electrospinning processes.

296

297   **Fig. 3** Images of the modified triaxial electrospinning processes: (a) the triaxial

298   electrospinning system; (b) the connections of the working fluids and power supply to

299   the spinneret; (c) a typical electrospinning process for the preparation of F3; (d) the

300   compound droplet observed for F3 without an electrical charge; (e) the compound F3

301   Taylor cone which is observed after the application of a voltage (15 kV); (f) the

302   concave surface within the PP tube; and (g) the spreading of an outer solvent droplet

303   on the PP film and a stainless steel plate.

304

Table 1 Parameters of the preparation of the four types of nanofibers. The outer fluid in all cases

comprised a mixture of acetone and acetic acid in a volume ratio of 2:1.

No.	Working process	Middle fluid [a] (wt%)	Fluid flow rate (mL/h)			Structure	Sheath thickness (nm)
			Outer	Middle	Inner [b]		
F1	Modified coaxial	0% CA	0.3	0.3	2	Monolithic	0
F2		1% CA	0.3	0.3	2	Core-shell	1.82
F3	Modified triaxial	3% CA	0.3	0.3	2	Core-shell	5.85
F4		5% CA	0.3	0.3	2	Core-shell	11.60

[a] The middle solution comprises CA in a mixture of acetone and acetic acid in a volume ratio of 2:1.

[b] The inner working fluid consisted of 4% (w/v) IBU and 16% (w/v) gliadin in a solvent mixture of HFIP and TFA (8:2 v/v).

3.3. Morphological characteristics and inner structures of the prepared nanofibers

All of the fibers prepared have linear and cylindrical morphologies with smooth surfaces (Fig. 4). No bead-on-a-string or spindle-on-a-string phenomena could be observed. As the concentration of CA in the middle working fluid increased from 0% w/v (F1) to 1% (F2), 3% (F3), and 5% (F4), the diameters of the nanofibers were raised from 0.54 ± 0.14 μm to 0.66 ± 0.13 μm, 0.72 ± 0.13 μm, and 0.87 ± 0.16 μm, respectively.

Natural polymers such as CA (and others such as zein and ethyl cellulose) are known to easily form a semi-solid substance at the nozzle of the spinneret during electrohydrodynamic processing, even at low concentrations (Li, et al., 2017; Yang, et al., 2018). Thus, in this study the outer solvent was used to prevent any clinging of semi-solid CA to the spinneret, preventing blocking of the needles and ensuring a stable and continuous electrospinning process. The outer solvent should also help the electrical forces to draw the inner and middle fluids evenly during the solvent exhaustion process (Yao, et al., 2018). These two effects of the outer solvent are

325   combined synergistially to ensure the formation of high-quality nanofibers regardless

326   of their composition (either monolithic F1 systems or core-shell hybrids in the case of

327   F2 to F4).
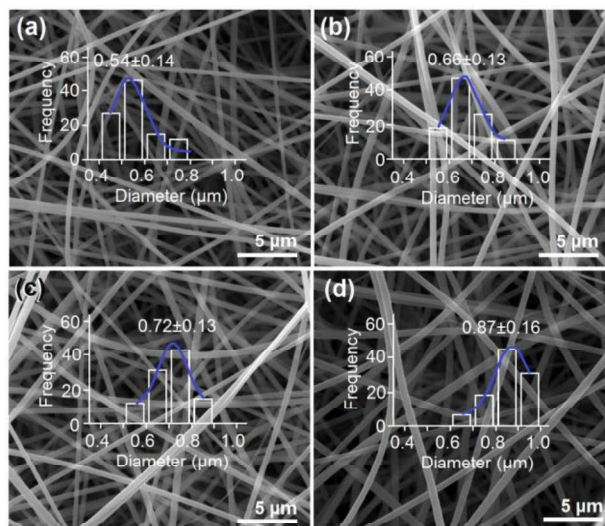
328

329   **Fig. 4** SEM images of the nanofibers prepared in this work: (a) F1; (b) F2; (c) F3; (d)

330   F4.

331   The internal structures of F1 to F4 were investigated by TEM (Fig. 5). F1

332   displays a gradual decrease in the gray contrast level moving from the center to the

333   two boundaries, as a result of the thicknesses of the fiber declining (Fig. 5a). No phase

334   separation can be seen. This indicates that the IBU molecules are highly dispersed

335   throughout the gliadin matrix on the molecular level, without any drug particles

336   forming.

337   The F2, F3, and F4 fibers, in contrast, had clear core-shell nanostructures (Fig.

338   5b-5d, respectively). The CA coating of F2 is too thin to be seen in the main TEM

339   image (Fig. 5b), but a line around 2 nm in thickness can be seen at the fiber exterior in

340   the inset image, indicating successful fabrication of a core/shell structure. The CA

341   coatings on F3 and F4 are clearer (see Fig. 5c and Fig. 5d), with estimated average

342   thicknesses of about 8 and 15 nm respectively. The CA coating for all of F2 – F4 is

343   evenly spread over the core IBU-gliadin composite. The outer solvent is thought to be

344   key in promoting such uniform coating during electrospinning.
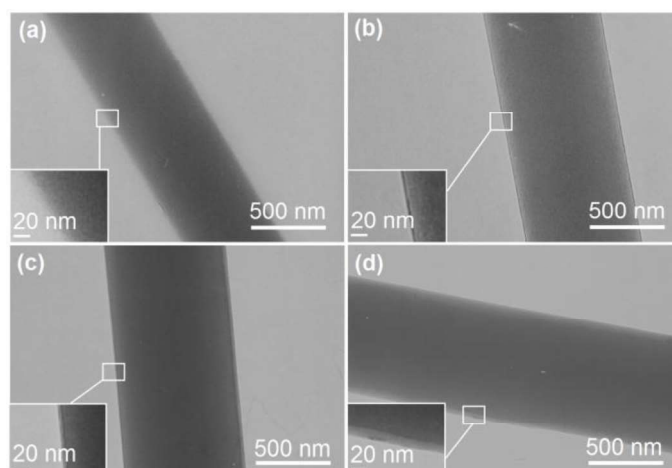
345

346   **Fig. 5** TEM images of the nanofibers: (a) F1; (b) F2; (c) F3; and (d) F4.

347   The average diameters of the nanofibers were determined using SEM images

348   (see Fig. 4) and found to be *ca.* 660, 720, and 870 nm for F2, F3, and F4 respectively.

349   Thus, the theoretical values of the different compartments' thickness can be estimated

350   based on the equation for the volume of a cylinder:

351
$$\frac{Q_s}{Q_c} = \frac{(R_f^2 - R_c^2)\rho_s L_f \pi}{R_c^2 \rho_c L_f \pi} = \frac{F_s \times C_s}{F_c \times C_c}$$

352   where Q, R, L, F, ρ and C represent the quantity of liquid dispensed, fiber radius, fiber

353   length, fluid flow rate, density, and solute concentration, respectively; and the

354   subscripts s, f, and c refer to the shell, the entire fiber, and the core. The L_f terms can

355   be cancelled, and R_c then calculated based the known values of R_f and the densities of

356   IBU-gliadin composite (*ca.* 0.878 g/cm^3) and CA (*ca.* 1.3 g/cm^3). For F2, F3, and F4,

357   this yields R_c values of 328.18, 354.15, and 423.40 nm, respectively. Thus, the CA

358   coating on fibers F2, F3, and F4 is estimated to be of 1.82, 5.85, and 11.60 nm in

359   thickness. The real thicknesses from the TEM images are slightly larger than these

360   calculated values. This is because, on one hand, the fast evaporation of solvent from

361   the surface of ejected fluids should make the shell CA coating have a smaller density

362   than usual. On the other hand, the medicated core nanocomposite might have a larger

363   density than both the IBU and gliadin. The filling effect of little IBU molecules in the

364   voids among gliadin molecules due to the favorable secondary interactions should

365   make the nanocomposites more compact than anticipation.

366   **3.4. Physical form of the components and component compatibility**

367   In the development of medicated nanomaterials of poorly water-soluble drugs, their

368   amorphous or crystalline state and their compatibility with carriers are vital for the

369   materials' functional performances and stability of long term preservation (Borbás,

370   et al., 2016; Démuth, et al., 2018). The XRD patterns of the raw material powders

371   (CA, gliadin, and IBU) and the electrospun nanofibers are shown in Fig. 6a. IBU is a

372   crystalline material, as demonstrated by a series of sharp Bragg reflections in its XRD

373   pattern. In contrast, the polymer CA and the protein matrix gliadin displayed no

374   Bragg reflections in their XRD patterns, suggesting that these materials were

375   amorphous in nature. The fibers have no Bragg reflections in their patterns, instead

376   exhibiting broad haloes indicating that they all comprise amorphous solid dispersions.

377   This is commonly observed in electrospun systems, because of the very rapid nature

378   of the drying process. The amorphous state of IBU in the fibers allows the tailoring of

379 its release profile, which can be controlled entirely by the polymer matrix in which it

380 is incorporated (rather than also being effected by the lattice enthalpy) (Kamaly,

381 Yameen, Wu, & Farokhzad, 2016; Démuth, et al., 2017; Jung, et al., 2018; Borbás, et

382 al., 2018; Wang, et al., 2018).
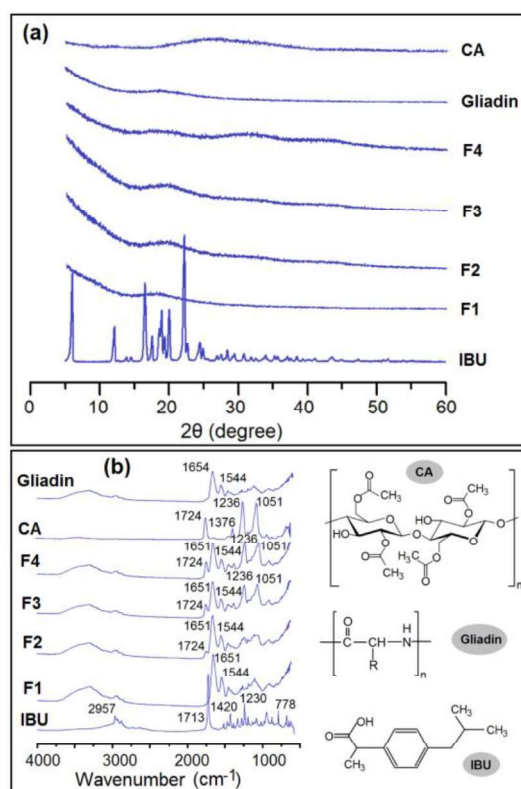
383

384 **Fig. 6** (a) XRD patterns of the raw materials and nanofibers, and (b) chemical

385 structures of the fiber components and their IR spectra

386   The chemical structures of the raw materials (CA, gliadin, and IBU), their IR

387 spectra, and the spectra of the nanofibers are given in Fig. 6b. The spectra of IBU

388 shows a characteristic peak at 1713 cm^{-1}, which corresponds to the stretching

389 vibrations of its –C=O groups. However, this peak disappeared from the spectrum of

390 the IBU-gliadin fiber F1. The lack of IR signs of IBU groups can be attributed to

391 several reasons, including its lower concentration in the fibers, the peak broadening

392   effect of the amorphous form, and also the secondary interactions between gliadin and

393   IBU. These interactions include hydrogen bonds with the protons provided by gliadin

394   molecules, hydrophobic interactions between the benzene rings of IBU and the carbon

395   skeletons of gliadin, and also the electrostatic interactions (Li, et al., 2018; Wang, et

396   al., 2018). It is just because of good compability between gliadin and CA in the

397   electrospun products, good compability between the working fluids containing

398   gliadin/IBU and CA for coaxial electrospinning, and that new excipients are highly

399   desired in pharmaceutics (Xu, et al., 2017) that gliadin was chosen as a carrier

400   polymer for IBU in the present study.

401   A comparison of the spectra of F2, F3, and F4 with that of F1 reveals that the

402   core-shell materials had some additional peaks, for instance at 1724, 1236, and 1051

403   cm^{-1}. These peaks are attributable to CA, and the F2 – F4 spectra can be regarded as

404   combinations of the CA and F1 spectra, indicating that the shell CA and the core

405   IBU-gliadin co-exist in F2 to F4 in a hybrid but not molecular composite manner. As

406   the thicknesses of the shell CA coating increases, the intensities of the characteristic

407   peaks of CA increase correspondingly. This observation can be closely related to use

408   of attenuated reflectance IR in these measurements: the penetration depth of the IR

409   probe in this technique is around 200 nm. Thus, the increase in the shell thickness

410   corresponds to a decrease in the amount of the core illuminated.

411   **3.5. In vitro drug release**

412   The in vitro IBU release profiles of the nanofibers are depicted in Fig. 7a. The period

413   of time taken for 100% release to be reached gradually increases as the thicknesses of

414   the CA coating increased from 0 nm in F1 to 1.82, 5.85, and 11.60 nm for nanofibers

415   F2, F3, and F4. An enlarged image of the IBU release in the first 2 h is shown in Fig.

416   7b. In the first hour, F1, F2, F3, and F4 release $34.2 \pm 4.5\%$, $8.3 \pm 4.6\%$, $5.4 \pm 4.1\%$,

417   and $2.7 \pm 3.1\%$ of the IBU loading respectively. The monolithic F1 material thus

418   shows a significant initial burst release. The core-shell nanohybrids F2 to F4 have

419   minimal initial bursts of release effects regardless of the thicknesses of the CA shell.

420   The CA coatings clearly improve the functional performance of the nanofibers in

421   terms of providing extended release durations and eliminating the initial burst release.

422   A zero-order equation was used to model the drug release data (Fig. 7c). For F1

423   to F4, the linear fit equations were $Q_1 = 24.89 + 6.94t$ ($R_1 = 0.8997$), $Q_2 = 10.36 +$

424    $3.19t$ ($R_2 = 0.9926$), $Q_3 = 5.34 + 2.41t$ ($R_3 = 0.9915$), and $Q_4 = 6.37 + 1.87t$ ($R_4 =$

425   0.9854), respectively. These correlation coefficients, in addition to visual inspection

426   of the plots in Fig. 7c demonstrate that while the core-shell hybrids F2 to F4 have

427   close to zero-order release, F1 very clearly does not.

428   The in vitro drug release data were further analyzed in accordance with the

429   power law expression to eludicate the drug release mechanisms (Peppas, 1985):

430    $Q = \dfrac{M_t}{M_\infty} = kt^n$

431    $\log Q = \log(\dfrac{M_t}{M_\infty}) = n\log(t) + \log(k)$

432   where M_t is the amount of drug released at time t, M_∞ is the total amount of drug in

433   the fibers, k is the rate constant, and n is a release exponent which is indicative of the

434   drug release mechanism. The regression equations for F1 to F4 (Fig. 7d) were $\log Q_1$

435 $= 1.56 + 0.41 \, log \, \text{t} \, (R_1 = 0.9911)$, $log \, Q_2 = 0.96 + 0.72 \, log \, \text{t} \, (R_2 = 0.9945)$, $log \, Q_3 =$

436 $0.71 + 0.80 \, log \, \text{t} \, (R_3 = 0.9976)$, and $log \, Q_4 = 0.49 + 0.90 \, log \, \text{t} \, (R_4 = 0.9961)$,

437 respectively. For F1, the exponent n was 0.41. This is smaller than the critical value of

438 0.45 (Peppas, 1985), suggesting that IBU was released through a typical Fickian

439 diffusion mechanism. However, all of the core-shell systems F2 to F4 had $n > 0.45$,

440 indicating a combination of diffusion and erosion mechanisms. However, the Peppas

441 power equation assumes that the drug is homogeneously distributed in the polymer

442 matrix, which is not the case for F2 - F4. Given that both CA and gliadin are insoluble

443 in water, it must be the case that diffusion of the drug through the fibers is the major

444 barrier to release, but the presence of the core/shell architecture confounded the

445 Peppas analysis.
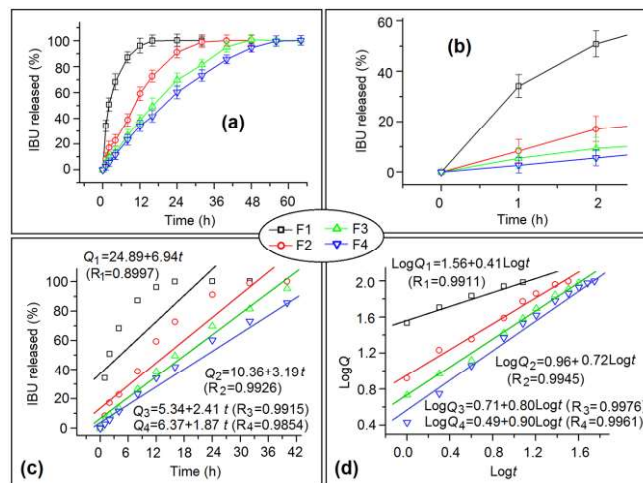
447 **Fig. 7** In vitro dissolution test results (a) throughout the experimental duration and (b)

448 for the first 2 h (b). Data are shown as mean ± S.D. from 6 independent experiments.

449 Fits to the IBU release data with (c) zero-order release kinetics and (d) the Peppas

450 power law expression are also shown.

451 **3.6. Process–nanostructure–performance relationship**

21

452 The core-shell nanostructures developed in this work could be effectively designed by

453 controlling the fluids in the modified triaxial electrospinning processes. Their

454 functional performance is controlled by the CA concentration in the middle working

455 fluid. A linear equation can be developed (Fig. 8a) linking the CA coating thickness

456 (*T*) to the CA concentration (*C*): $T = -0.371 + 2.306\ C$ (R = 0.9947). It is thus

457 possible to precisely manipulate the coating thickness by varying the CA

458 concentration.

459   The CA layer thickness in turn has a major effect on the drug release behaviors

460 of the nanohybrids. The time taken for the release percentages to reach 30, 50, and

461 90% all increase with the coating thicknesses (Fig. 8b). The CA coating effectively

462 acts as a tool to control and tune the drug release rate from the core compartment.
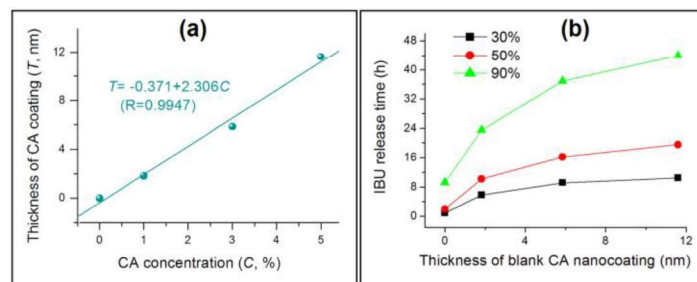
463

464 **Fig. 8** (a) The effect of the CA concentrations in the middle working fluid on the

465   thicknesses of the fiber coating and (b) the variation in IBU release profiles with the

466   CA coating depth (showing the time taken to reach 30, 50, and 90% release).

467   In conventional medicines, a crystalline drug is dispersed in a carrier matrix, and

468 the physical and chemical properties of the latter control the drug release properties *in*

469 *vivo* (Qi & Craig, 2016). In the development of electrospun nanofibers via traditional

470 monoaxial blend electrospinning, drug molecules are uniformly distributed

471 throughout a filament-forming matrix in the form of an amorphous solid dispersion,

472   as is the case for F1 in this study (Fig. 9). As a result, a burst release of drug is

473   observed, since the fibers have large surface areas and a significant proportion of the

474   drug is near the surface and so can dissolve into solution rapidly. When the blank CA

475   coating was added to the IBU/gliadin core in the modified triaxial electrospinning

476   process, this modulated the drug release behavior. A thicker CA coating layer (e.g. in

477   F4 cf. F2) could extend the drug release duration to a greater extent (Fig. 9). The F2 -

478   F4 formulations can be regarded as reservoir-type drug delivery systems, with the CA

479   layer controlling the release properties. A process–nanostructure–performance

480   relationship can hence be determined. This relationship could be used to develop new

481   types of functional nanomaterials allowing individualized administration ensuring

482   patients receive safe, effective, and economical treatments.
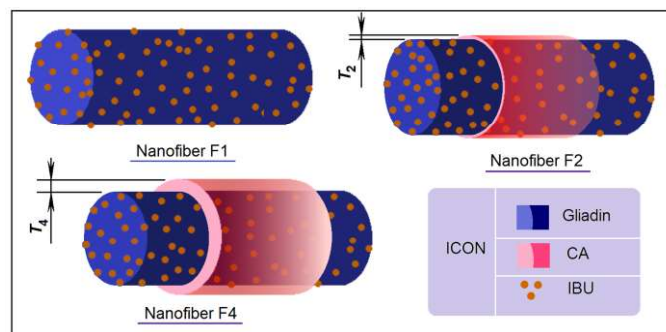
484   **Fig. 9** The core-shell structures of the fibers and drug distributions within them.

485   **4. Conclusions**

486   A modified triaxial electrospinning process was successfully developed in this

487   work and used to prepare a series of core-shell nanohybrids. The three fluids used for

488   electrospinning comprised a plain solvent (outer fluid), a non-electrospinnable dilute

489   cellulose acetate (CA) solution (middle) and an electrospinnable ibuprofen-gliadin

490   solution (inner fluid). This led to the formation of ibuprofen/gliadin amorphous solid

491   dispersions coated with a thin layer of CA. The thickness of the coating could be

492   precisely tuned through the CA concentration in the middle solution. SEM and TEM

493   images revealed that the fibers had linear and cylindrical morphologies with a clear

494   core-shell nanostructure. The IBU in the nanofibers was amorphously distributed

495   throughout the core matrix, thought to be because it is able to form intermolecular

496   interactions with gliadin. In vitro dissolution tests showed an initial burst release to

497   arise from monolithic ibuprofen/gliadin fibers, but this was completely eliminated in

498   the systems with a CA coating. The coating also extended the release duration, with a

499   thicker coating layer leading to longer release times. This study hence provides a new

500   way to develop advanced functional nanomaterials and to control their properties via

501   process–nanostructure–performance relationships in triaxial electrospinning.

502

503   **Conflict of interest**

504   The authors have no conflicts of interest to declare.

505   **Acknowledgements**

509

510   **References**

511   Acharya, M., Mishra, S., Sahoo, R. N., & Mallick, S. (2017). Infrared spectroscopy
512   for analysis of co-processed ibuprofen and magnesium trisilicate at milling and
513   freeze drying. *Acta Chimica Slovenica, 64*(1), 45-54.
514   Agarwal, S., Greiner, A., & Wendorff, J. H. (2013). Functional materials by

515   electrospinning of polymers. *Progress in Polymer Science, 38*(6), 963-991.

516   Borbás, E., Nagy, Z. K., Nagy, B., Balogh, A., Farkas, B., Tsinman, O., et al. (2018).
517   The effect of formulation additives on in vitro dissolution-absorption profile and
518   in vivo bioavailability of telmisartan from brand and generic
519   formulations. *European Journal of Pharmaceutical Sciences, 114*, 310-317.

520   Borbás, E., Sinkó, B., Tsinman, O., Tsinman, K., Kiserdei, E., Démuth, B., et al.
521   (2016). Investigation and mathematical description of the real driving force of
522   passive transport of drug molecules from supersaturated solutions. *Molecular*
523   *pharmaceutics, 13*(11), 3816-3826.

524   Chang, Y., He, L., Li, Z., Zeng, L., Song, Z., Li, P., et al. (2017). Designing core-shell
525   gold and selenium nanocomposites for cancer radiochemotherapy. *ACS Nano,*
526   *11*(5), 4848-4858.

527   Chaudhuri, R. G., & Paria, S. (2012). Core/shell nanoparticles: Classes, properties,
528   synthesis mechanisms, characterization, and applications. *Chemical Reviews,*
529   *112*(4), 2373-2433.

530   Démuth, B., Galata, D. L., Balogh, A., Szabó, E., Nagy, B., Farkas, A., et al. (2018).
531   Application of hydroxypropyl methylcellulose as a protective agent against
532   magnesium stearate induced crystallization of amorphous itraconazole. *European*
533   *Journal of Pharmaceutical Sciences*, 121, 301-308.

534   Démuth, B., Galata, D. L., Szabó, E., Nagy, B., Farkas, A., Balogh, A., et al. (2017).
535   Investigation of deteriorated dissolution of amorphous itraconazole: Description
536   of incompatibility with magnesium stearate and possible solutions. *Molecular*
537   *pharmaceutics, 14*(11), 3927-3934.

538   Eltayeb, M., Stride, E., & Edirisinghe, M. (2013). Electrosprayed core-shell
539   polymer-lipid nanoparticles for active component delivery. *Nanotechnology,*
540   *24*(46), 465604.

541   Habiba, U., Siddique, T. A., Lee, J. J. L., Joo, T. C., Ang, B. C., & Afifi, A. M.
542   (2018). Adsorption study of methyl orange by chitosan/polyvinyl alcohol/zeolite
543   electrospun composite nanofibrous membrane. *Carbohydrate polymers, 191*,
544   79-85.

545   Haider, S., Ali, F. A. A., Haider, A., Al-Masry, W. A., & Al-Zeghayer, Y. (2018).
546   Novel route for amine grafting to chitosan electrospun nanofibers membrane for
547   the removal of copper and lead ions from aqueous medium. *Carbohydrate*
548   *Polymers*, https://doi.org/10.1016/j.carbpol.2018.07.026.

549   Han, D., Sherman, S., Filocamo, S., & Steckl, A. J. (2017). Long-term antimicrobial
550   effect of nisin released from electrospun triaxial fiber membranes. *Acta*
551   *biomaterialia, 53*, 242-249.

552   Han, D., & Steckl, A. J. (2013). Triaxial electrospun nanofiber membranes for
553   controlled dual release of functional molecules. *ACS Applied Materials &*
554   *Interfaces, 5*(16)*,* 8241-8245.

555   He, M., Jiang, H., Wang, R., Xie, Y., & Zhao, C. (2017). Fabrication of
556   metronidazole loaded poly(ε-caprolactone)/zein core/shell nanofiber membranes
557   via coaxial electrospinning for guided tissue regeneration. *Journal of Colloid and*
558   *Interface Science, 490*, 270-278.

559   Hubbell, J. A., & Chikoti, A. (2012). Nanomaterials for drug delivery. *Science, 337*
560   (6092), 303-305.

561   Isaacoff, B. P., & Brown, K. A. (2017). Progress in top-down control of bottom-up
562   assembly. *Nano Letters, 17*(11), 6508-6510.

563   Jiang, S., Chen, Y., Duan, G., Mei, C., Greiner, A., & Agarwal, S. (2018).
564   Electrospun nanofiber reinforced composites: a review. *Polymer Chemistry,*

9(20), 2685-2720.

Jiang, S., Duan, G., Zussman, E., Greiner, A., & Agarwal, S. (2014). Highly flexible and tough concentric tri-axial polystyrene fibers. *ACS Applied Materials & Interfaces*, *6*(8), 5918-5923.

Jiang, S., Uch, B., Agarwal, S., & Greiner, A. (2017). Ultralight, thermally insulating, compressible polyimide fiber assembled sponges. *ACS applied materials & interfaces*, *9*(37), 32308-32315.

Jung, H. S., Kim, M. H., Shin, J. Y., Park, S. R., Jung, J. Y., & Park, W. H. (2018). Electrospinning and wound healing activity of β-chitin extracted from cuttlefish bone. *Carbohydrate polymers*, *193*, 205-211.

Kamaly, N., Yameen, B., Wu, J., & Farokhzad, O. C. (2016). Degradable controlled-release polymers and polymeric nanoparticles: mechanisms of controlling drug release. *Chemical reviews*, *116*(4), 2602-2663.

Khoshnevisan, K., Maleki, H., Samadian, H., Shahsavari, S., Sarrafzadeh, M. H., Larijani, B., et al. (2018). Cellulose acetate electrospun nanofibers for drug delivery systems: Applications and recent advances. *Carbohydrate Polymers, 198*, 131-141.

Labbaf, S., Ghanbar, H., Stride, E., & Edirisinghe, M. (2014). Preparation of multilayered polymeric structures using a novel four-needle coaxial electrohydrodynamic device. *Macromolecular Rapid Communications*, *35*(6), 618-623.

Lallave, M., Bedia, J., Ruiz- Rosas, R., Rodríguez- Mirasol, J., Cordero, T., Otero, J. C., et al. (2007). Filled and hollow carbon nanofibers by coaxial electrospinning of alcell lignin without binder polymers. *Advanced Materials*, *19*(23), 4292-4296.

Lauhon, L. J., Gudiksen, M. S., Wang, D., & Lieber, C. M. (2002). Epitaxial core-shell and core-multishell nanowire heterostructures. *Nature, 420*(6911), 57-61.

Li, J. J., Yang, Y. Y., Yu, D. G, Du Q., & Yang, X. L. (2018). Fast dissolving drug delivery membrane based on the ultra-thin shell of electrospun core-shell nanofibers. *European Journal of Pharmaceutical Sciences*, *122*, 195-204.

Li, X. Y., Zheng, Z. B., Yu, D. G., Liu, X. K., Qu, Y. L., & Li, H. L. (2017). Electrosprayed sperical ethylcellulose nanoparticles for an improved sustained-release profile of anticancer drug. *Cellulose*, *24*(12), 5551-5564.

Liao, Y., Loh, C. H., Tian, M., Wang, R., & Fane, A. G. (2018). Progress in electrospun polymeric nanofibrous membranes for water treatment: Fabrication, modification and applications. *Progress in Polymer Science*, 77, 69-94.

Liu, W., Ni, C., Chase, D. B., & Rabolt, J. F. (2013). Preparation of multilayer biodegradable nanofibers by triaxial electrospinning. *ACS Macro Letters*, *2*(6), 466-468.

Lu, Y., Xiao, X., Zhan, Y., Huan, C., Qi, S., Cheng, H., & Xu, G. (2018). Core-sheath paraffin-wax-loaded nanofibers by electrospinning for heat storage. *ACS Applied Materials & Interfaces*, *10*(15), 12759-12767.

Mao, Z., Li, J., Huang, W., Jiang, H., Zimba, B. L., Chen, L., et al. (2018). Preparation of poly (lactic acid)/graphene oxide nanofiber membranes with different structures by electrospinning for drug delivery. *RSC Advances, 8*(30), 16619-16625.

Masoumifard, N., Guillet-Nicolas, R., & Kleitz, F. (2018). Synthesis of engineered zeolitic materials: From classical zeolites to hierarchical core-shell materials. *Advnced Materials*, *30*(16), 1704439.

615 Mehta, P., Haj-Ahmad, R., Rasekh, M., Arshad, M. S., Smith, A., van der Merwe, S.
616   M., & Ahmad, Z. (2017). Pharmaceutical and biomaterial engineering via
617   electrohydrodynamic atomization technologies. *Drug Discovery Today*, *22*(1),
618   157-165.
619 Mitragotri, S., Burke, P. A., & Langer, R. (2014). Overcoming the challenges in
620   administering biopharmaceuticals: Formulation and delivery strategies. *Nature*
621   *reviews Drug discovery*, *13*(9), 655-672.
622 National Pharmacopoeia Committee (2015). Pharmacopoeia of People's Republic of
623   China. Part 4. Beijing: China Medical Science and Technology Press, page 121.
624 Nie, H., Fu, Y., & Wang, C. H. (2010). Paclitaxel and suramin-loaded core/shell
625   microspheres in the treatment of brain tumors. *Biomaterials*, *31*(33), 8732-8740.
626 Peppas, N. A. (1985). Analysis of Fickian and non-Fickian drug release from
627   polymers. *Pharmaceutica Acta Helvetia*e, *60*(4), 110-111.
628 Qi, S., & Craig, D. (2016). Recent developments in micro-and nanofabrication
629   techniques for the preparation of amorphous pharmaceutical dosage
630   forms. *Advanced Drug Delivery Reviews*, *100*, 67-84.
631 Qu, H., Wei, S., & Guo, Z. (2013). Coaxial electrospun nanostructures and their
632   applications. *Journal of Materials Chemistry A*, *1*(38), 11513-11528.
633 Starr, J. D., Budi, M. A. K., & Andrew, J. S. (2015). Processing-property relationships
634   in electrospun Janus-type biphasic ceramic nanofibers. *Journal of the American*
635   *Ceramic Society, 98*(1), 12-19.
636 Szabó, E., Démuth, B., Nagy, B., Molnár, K., Farkas, A., Szabó, B., et al. (2018).
637   Scaled-up preparation of drug-loaded electrospun polymer fibres and
638   investigation of their continuous processing to tablet form. *Express Polymer*
639   *Letters*, *12*(5), 436-451.
640 Wali, A., Zhang, Y., Sengupta, P., Higaki, Y., Takahara, A., & Badiger, M. V. (2018).
641   Electrospinning of non-ionic cellulose ethers/polyvinyl alcohol nanofibers:
642   Characterization and applications. *Carbohydrate polymers*, *181*, 175-182.
643 Wang, K., Liu, X. K., Chen, X. H., Yu, D. G., Yang, Y. Y., & Liu, P. (2018).
644   Electrospun hydrophilic Janus nanocomposites for the rapid onset of therapeutic
645   action of helicid. *ACS applied materials & interfaces*, *10*(3), 2859-2867.
646 Wang, K., Wen, H. F., Yu, D. G., Yang, Y. Y., & Zhang, D. F. (2018). Electrosprayed
647   hydrophilic nanocomposites coated with shellac for colon-specific delayed drug
648   delivery. *Materials & Design*, *143*, 248-255.
649 Wang, Q., Yu, D. G., Zhang, L. L., Liu, X. K., Deng, Y. C., & Zhao, M. (2017).
650   Electrospun hypromellose-based hydrophilic composites for rapid dissolution of
651   poorly water-soluble drug. *Carbohydrate Polymers, 174*, 617-625.
652 Wang, Q., Yu, D. G., Zhou, S. Y., Li, C., & Zhao, M. (2018). Electrospun amorphous
653   medicated nanocomposites fabricated using a Teflon-based concentric
654   spinneret. *e-Polymers*, *18*(1), 3-11.
655 Wen, P., Wen, Y., Huang, X., Zong, M. H., & Wu, H. (2017). Preparation and
656   characterization of protein-loaded electrospun fiber mat and its release kinetics.
657   *Journal of Agricultural & Food Chemistry*, *65*(23), 4786-4796.
658 Xu, Y., Li, J. J., Yu, D. G., Williams, G. R., Yang, J. H., & Wang, X. (2017). Influence
659   of the drug distribution in electrospun gliadin fibers on drug-release behavior.
660   *European Journal of Pharmaceutical Sciences, 106*, 422-430.
661 Yang, C., Yu, D. G., Pan, D., Liu, X. K., Wang, X., Bligh, S. A., & Williams, G. R.
662   (2016). Electrospun pH-sensitive core-shell polymer nanocomposites fabricated
663   using a tri-axial process. *Acta biomaterialia*, *35*, 77-86.
664 Yang, G. Z., Li, J. J., Yu, D. G., He, M. F., Yang, J. H., & Williams, G. R. (2017).

Nanosized sustained-release drug depots fabricated using modified tri-axial electrospinning. *Acta biomaterialia*, *53*, 233-241.

Yang, Y. Y., Zhang, M., Liu, Z. P., Wang, K., & Yu, D. G. (2018). Meletin sustained-release gliadin nanoparticles prepared via solvent surface modification on blending electrospraying. *Applied Surface Science*, *434*, 1040-1047.

Yao, Z. C., Zhang, C., Ahmad, Z., Huang, J., Li, J. S., & Chang, M. W. (2018). Designer fibers from 2D to 3D-Simultaneous and controlled engineering of morphology, shape and size. *Chemical Engineering Journal*, *334*, 89-98.

You, M. H., Wang, X. X., Yan, X., Zhang, J., Song, W. Z., Yu, M., et al. (2018). A self-powered flexible hybrid piezoelectric–pyroelectric nanogenerator based on non-woven nanofiber membranes. *Journal of Materials Chemistry A, 6*(8), 3500-3509.

Yu, D.G., Li, J. J., Williams, G. R., & Zhao, M. (2018). Electrospun amorphous solid dispersions of poorly water-soluble drugs: A review. *Journal of Controlled Release*, 2018, https://doi.org/10.1016/j.jconrel.2018.08.016

Zanjani, J. S. M., Okan, B. S., Yilmaz, C., Menceloglu, Y., & Yildiz, M. (2017). Monitoring the interface and bulk self-healing capability of tri-axial electrospun fibers in glass fiber reinforced epoxy composites. *Composites Part A: Applied Science and Manufacturing*, *99*, 221-232.

Zhao, Y., Cao, X., & Jiang, L. (2007). Bio-mimic multichannel microtubes by a facile method. *Journal of the American Chemical Society, 129*(4), 764-765.